Proceedings of the Combustion Institute 42 (2026) 106244

Contents lists available at ScienceDirect

Proceedings of the Combustion Institute

journal homepage: www.elsevier.com/locate/proci

In situ X-ray absorption spectroscopy and multispectral pyrometry for spatially resolved probing of iron oxide phase evolution and temperature in iron dust flames

Fabian P. Hagen [a,*], Lukas Braun [b,c], Dmitry E. Doronkin [b,c], Malte Seitz [a], Michal Fedoryk [a], Björn Stelzner [a], Jan-Dierk Grunwaldt [b,c], Dimosthenis Trimis [a]

[a] Engler-Bunte-Institute, Combustion Technology, Karlsruhe Institute of Technology (KIT), Germany
[b] Institute for Chemical Technology and Polymer Chemistry, Karlsruhe Institute of Technology (KIT), Germany
[c] Institute of Catalysis Research and Technology, Karlsruhe Institute of Technology (KIT), Germany

ARTICLE INFO

Keywords:
X-ray absorption spectroscopy
In situ diagnostics
Synchrotron
Iron oxide phase evolution
Particle temperature

ABSTRACT

This study reports spatially resolved, coupled quantification of iron (oxide) phase evolution and particle temperature in laminar iron dust flames of Bunsen-type using synchrotron-based *in situ* X-ray absorption spectroscopy (XAS) and multispectral pyrometry. Line-of-sight (LOS) XAS measurements at the Fe K-edge were evaluated by linear combination analysis (LCA) to obtain LOS molar fractions of Fe, FeO, and Fe_3O_4, which were subsequently reconstructed into local radial distributions using inverse Abel transformation. Simultaneously, multispectral pyrometry provided spatially resolved particle ensemble temperatures, enabling direct correlation between local chemical and thermal states. The coupled measurements reveal a two-step oxidation sequence: conversion of Fe to FeO coincides with the high-temperature reaction front, followed by subsequent formation of Fe_3O_4 in the post-flame region. With increasing oxygen concentration in the oxidizer from 19 vol.% to 25 vol.% O_2, particle temperatures in the reaction front increase from about 2140 K to 2350 K, resulting in nearly complete conversion of Fe within the investigated region. Variations in equivalence ratio induce minor changes in iron oxide phase evolution, likely associated with particle loading, whereas the temperature field shows limited sensitivity within the investigated range. Beyond resolving the spatial coupling of particle temperature and oxidation state, the multimodal diagnostic approach establishes a transferable framework for quantitative, non-intrusive probing of iron dust flames and, combined with previously reported nanoparticle size distributions, provides a data set linking particle temperature, phase composition, and nanoparticle formation for validation and development of predictive models.

Novelty and significance statement.

To date, only one study, by Sperling et al. [1], has tracked the phase evolution of iron oxides under flame-like high-temperature oxidation conditions, relying on *ex situ* analysis of quenched particles from a single particle experiment. Here, we report, to our knowledge, the first *in situ* quantification of the evolution of iron (oxide) phases and particle temperature in laminar iron dust flames by combining synchrotron X-ray absorption spectroscopy (XAS) with multispectral pyrometry. By non-intrusive probing of correlated thermal and chemical state information, this approach provides evidence for a mechanistic link between the local flame environment and oxidation pathways. Together with previously reported nanoparticle size distributions [2], this study provides a benchmark data set on particle temperature, phase composition, and nanoparticle formation for model validation. In addition, the presented methodology establishes a transferable diagnostic framework applicable across varying particle sizes, boundary conditions, and burner configurations.

1. Introduction

Micron-sized iron particles have emerged as promising carbon-free energy carriers, enabling a closed iron–hydrogen redox cycle for renewable energy storage [3,4]. In this concept, hydrogen reduces iron oxide to metallic iron particles, while subsequent iron combustion releases heat and forms iron oxides, closing the cycle [5].

* Corresponding author.
E-mail address: fabian.hagen@kit.edu (F.P. Hagen).

https://doi.org/10.1016/j.proci.2026.106244
Received 15 March 2026; Accepted 7 June 2026
Available online 9 July 2026

While iron combustion has attracted growing attention, the high-temperature oxidation behavior of micron-sized iron particles and the underlying phase-selective reaction kinetics remain only partially understood.

Single particle studies have provided insights into particle ignition [6], burning times [7–9], melting [8,10,11], temperature histories [10,12], size evolution [8,13], and nanoparticle formation [11,14,15], yet provide only limited and indirect access to phase-resolved oxidation kinetics. Investigations of particle ensembles in model flames – such as Bunsen-type, counterflow, lifted, and hybrid CH_4/iron configurations – have enabled the characterization of laminar burning velocities [16–19], while recent work has revealed the spatial evolution of nanoparticle size distributions [2]. However, the *in situ* quantification of the iron oxide phase composition at high temperature remains elusive. To date, phase analysis relies on *ex situ* characterization of sampled particles [1,20,21], which may lose information on high-temperature oxide states.

To address these knowledge gaps, the iron oxide phase composition in iron dust flames is investigated using *in situ* X-ray absorption spectroscopy (XAS), an element-specific method probing local atomic structure and oxidation states of iron [22,23]. Measurements were conducted at beamline P64 [24,25] of PETRA III at the Deutsches Elektronen-Synchrotron (DESY) [26] in Hamburg, Germany. Complementary multispectral pyrometry was performed at the synchrotron facility to determine particle temperatures, enabling correlation with phase evolution. The study examines how equivalence ratio, Φ, and oxygen concentration, $[O_2]$, in the oxidizer influence particle temperature and, consequently, iron oxide phase evolution in iron dust flames, providing key experimental data relevant for validation of recent modeling studies on iron dust combustion; see, *e.g.*, [27–30].

2. Experimental approach

This section outlines the experimental setup for *in situ* XAS and multispectral pyrometry used to quantify iron oxide phase evolution and particle temperatures in iron dust flames, including the Bunsen-type burner setup and the investigated flame conditions.

2.1. In situ XAS at the Fe K-edge

XAS at the Fe K-edge probes electronic transitions from Fe 1s core level primarily into unoccupied 4p states and continuum, providing element-specific sensitivity to oxidation state and local coordination. Consequently, the energy position and fine structure of the absorption edge allow distinction between metallic and oxidized iron species. To determine these oxidation states within the laminar iron dust flames of Bunsen-type, *in situ* XAS was performed in transmission mode. Based on the Lambert–Beer law, the energy-dependent X-ray absorption coefficient $\mu(E)$ is obtained from the incident and transmitted beam intensities I_0 and I_1 via

$$\mu(E)\,\ell(x) = \ln\left(I_0\, I_1^{-1}\right), \tag{1}$$

where $\ell(x)$ denotes the X-ray path length through the flame at a distance x from the flame centerline. Owing to the cylindrical symmetry of the flame, it follows geometrically that $\ell(x) = 2\sqrt{R^2 - x^2}$, with R being the outer flame radius.

In situ XAS measurements were performed at beamline P64 [24] at DESY using a quick-scanning extended X-ray absorption fine structure (QEXAFS) monochromator [25] operated at 5 Hz. The setup, equipped with two ionization chambers and a passivated implanted planar silicon (PIPS) diode for a reference iron foil, enabled simultaneous detection of I_0, I_1, and the reference signal I_{ref} for energy calibration and drift correction. A CMOS camera provided real-time flame visualization for flame front localization and measurement positioning.

Line-of-sight (LOS) *in situ* XAS probing was conducted at >30 positions to reconstruct 2D maps of iron and its oxides up to a flame height of 7 cm. Measurements were performed at multiple radial positions over more than half of the region of interest (ROI), extending beyond the visible flame tip. In the outer radial regions at larger heights, dilution of the aerosol by the coflow reduced the particle concentration and thereby the signal-to-noise ratio (SNR). In this region, the phase composition was linearly extrapolated at selected positions from the centerline measurements toward the outer radial regions to enable visualization of the complete 2D phase distribution only.

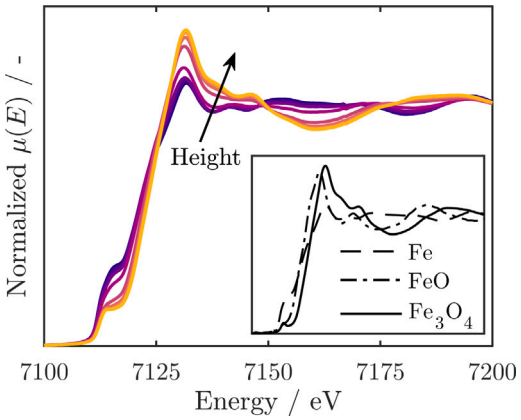

Fig. 1. Centerline XAS spectra reconstructed from inverse Abel-transformed LCA data of stoichiometric flame #2 for flame heights of $0, 1, \ldots, 7$ cm, with color indicating increasing height from blue to yellow, together with reference spectra of Fe, FeO, and Fe_3O_4.

Additionally, XAS spectra of selected reference samples, *i.e.*, Fe, FeO, and Fe_3O_4, were recorded using an identical configuration of the beamline optics and are shown in Fig. 1. Probed LOS XAS spectra were analyzed by linear combination analysis (LCA) using these spectra as reference components to quantify the molar fractions of Fe, FeO, and Fe_3O_4. Fe_2O_3 was deliberately excluded from the LCA, as it is not expected to form under the conditions present in the ROI. The maximum molar oxygen-to-iron ratio determined for flame #6 with 25 vol.% O_2 in the oxidizer, see Table 1, was approx. 1.2, well below the stability limit of Fe_2O_3 as indicated by the phase diagram reported by Sperling et al. [1]. Although Fe(II) features in Fe_3O_4 could in principle arise from a mixture of minor fractions of FeO and Fe_2O_3, this is unlikely given the prevailing experimental conditions; further discussion is provided in Section 3.

The LOS molar fractions obtained from LCA were subsequently reconstructed into local radial phase distributions by inverse Abel transformation. Owing to the radial symmetry of the flame, this reconstruction yields spatially resolved information across the flame cross section. The inverse Abel transformation was performed using a discretized chord-length formulation with Tikhonov regularization. To suppress numerical noise, the reconstructed fields were smoothed using a Gaussian filter and interpolated onto a refined spatial grid for visualization. Reconstruction consistency was verified by forward projection, yielding negligible deviations from the measured LOS-integrated data. Fig. 1 shows centerline spectra reconstructed from the inverse Abel-transformed LCA data of the stoichiometric flame, see #2 in Table 1. The spectral shape gradually evolves from metallic Fe near the burner exit toward iron oxides with increasing height, indicating progressive oxidation.

The uncertainty of the phase quantification is primarily governed by temporal fluctuations of the measured spectra and amounts to approx. 5% near the flame front across all investigated conditions, while reaching about 10% in the post-flame regions of the ROI due to decreasing SNR.

The experimental setup for *in situ* XAS, representative flame images highlighting the investigated ROI, and the probing positions are shown in Fig. 2.

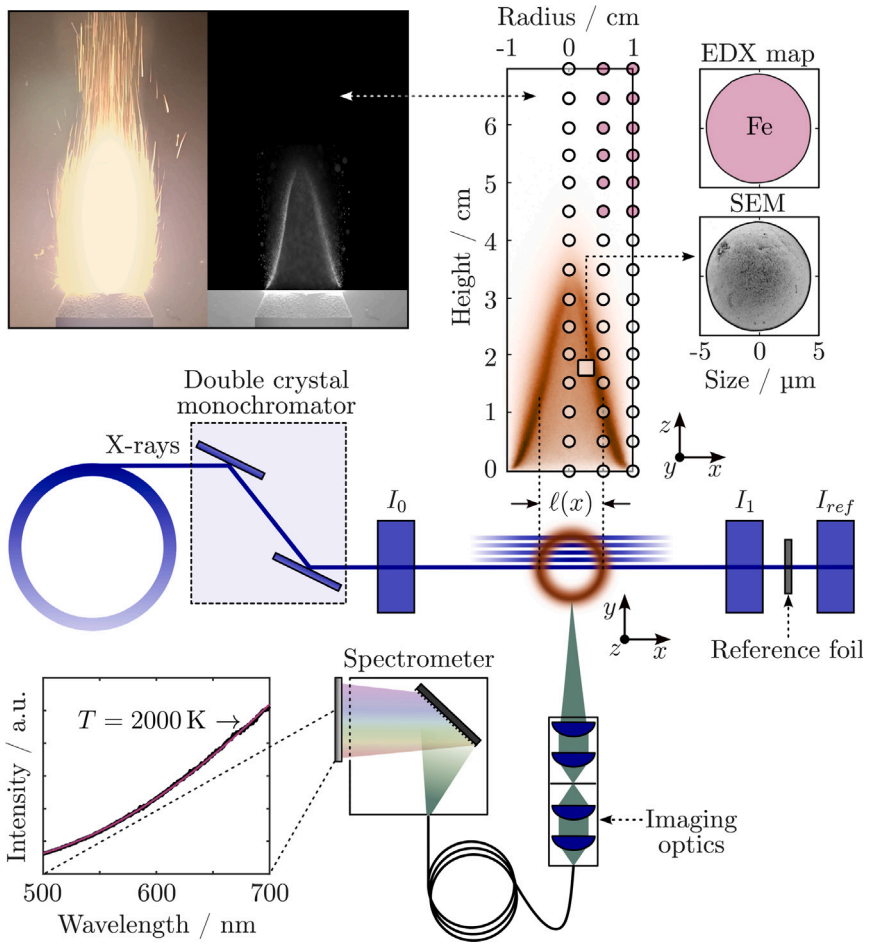

Fig. 2. Experimental setup for *in situ* XAS and multispectral pyrometry in iron dust flames of Bunsen-type. Representative flame images are shown, highlighting the investigated region of interest (ROI). White circles indicate *in situ* XAS measurement positions, whereas red circles denote extrapolated points. Emission spectra were recorded at all positions using multispectral pyrometry. A scanning electron microscopy (SEM) image of a representative iron particle is shown together with the corresponding energy-dispersive X-ray (EDX) map of its cross section, revealing a spherical, dense, micron-sized particle composed of pure iron. An exemplary fit of Planck's law to a measured spectrum of flame #4, see Table 1, and the resulting particle ensemble temperature T within the probe volume are also displayed.

Table 1
Investigated laminar iron dust flames of Bunsen-type; see Section 2.4 and Supplementary Material for details.

Flame	Φ/–	$[O_2]$/vol.%
#1	0.80	21
#2	1.00	21
#3	1.25	21
#4	1.00	19
#5	1.00	23
#6	1.00	25

2.2. Multispectral pyrometry

Particle temperatures were determined by multispectral pyrometry [31,32], where the detected radiation represents the ensemble emission of particles traversing the probe volume. For reacting micron-sized iron (oxide) particles, Biot numbers are below unity [12], indicating that internal temperature gradients are expected to be small. Under these conditions, the particle surface temperature, which governs the emitted thermal radiation, can be approximated as spatially uniform across each particle.

The optical setup is illustrated in Fig. 2. Radiation emitted from a defined position within the iron dust flame was collected by an imaging lens. The intermediate image was spatially filtered by a pinhole located in the image plane, thereby restricting the measurement volume. The transmitted radiation was subsequently collimated and focused into an optical fiber guiding the signal to a Czerny–Turner spectrograph equipped with a CCD detector. The effective probe volume defined by the imaging optics and pinhole results in a spatial resolution of approx. 400 µm. The measurement locations correspond to the positions used for the *in situ* XAS; radial profiles were obtained only at integer heights, while the centerline was probed at all positions.

The background-corrected spectral intensity I_λ is determined by the particle emissivity and the wavelength-dependent response of the optical system and can be written as

$$I_\lambda = C(\lambda)\,\varepsilon_\lambda\,B(\lambda,T), \tag{2}$$

where $C(\lambda)$ denotes the spectral response function, ε_λ the particle emissivity, and $B(\lambda,T)$ the spectral radiance given by Planck's law,

$$B(\lambda,T) = \frac{2hc^2}{\lambda^5}\left[\exp\left(\frac{hc}{\lambda k_B T}\right) - 1\right]^{-1}, \tag{3}$$

with h being Planck's constant, c the speed of light, k_B the Boltzmann constant, and T the particle temperature.

The spectral response function $C(\lambda)$ was determined using a calibrated tungsten ribbon lamp. After correction, the particle temperature was obtained by non-linear least-squares fitting of Planck's law to the emission spectra assuming gray body behavior, *i.e.*, ε_λ = const.

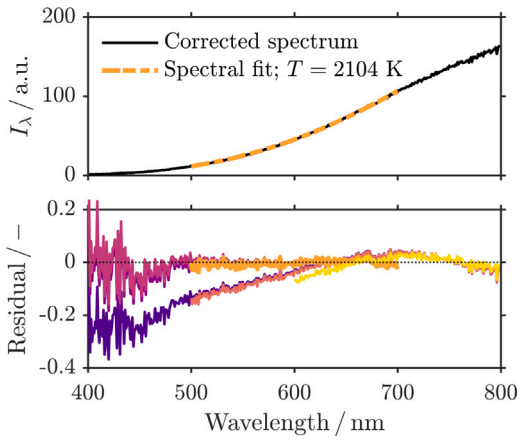

Fig. 3. Corrected emission spectrum from the centerline of flame #2 at a height of 3 cm corresponding to the reaction front together with the spectral fit according to Eq. (2). The residual between measurement and fit is shown for six investigated wavelength intervals, indicated by the different colors. The orange line marks $\Delta\lambda_{opt}$.

This assumption is critical here, since the emissivity of reacting iron (oxide) particles is generally unknown and may vary with wavelength as particle composition and size evolve. In the present study, the particles are therefore approximated as gray bodies within a limited spectral interval. The quality of the spectral fit was used to assess this approximation: close agreement between the measured spectrum and the fit based on Eq. (2) indicates that the gray body assumption is reasonable within the selected spectral interval, whereas systematic deviations point to wavelength-dependent emissivity effects that limit the accuracy of the temperature evaluation. An example of this residual analysis is shown in Fig. 3. The upper panel presents a measured emission spectrum from the centerline at a height of 3 cm, corresponding to the reaction front, together with the spectral fit according to Eq. (2). The resulting particle temperature for this example is 2104 K. The lower panel shows the residual between the measured spectrum and the fitted curve for several spectral fitting intervals. A comparison reveals that, as in Ref. [12], $\Delta\lambda_{opt} = 500 \ldots 700$ nm yields the smallest residual, with a maximum deviation below about 4%. When other wavelength intervals are considered, the maximum deviation increases, reaching values of up to about 40% when shorter wavelengths are included, while the range between 600 nm and 800 nm results in deviations of roughly 10%. Although the inferred temperatures vary with the selected spectral interval, the differences remain moderate, amounting to about 7% for the cases shown in Fig. 3, indicating robust quantification. Based on this residual analysis, performed for multiple positions in both the reaction zone and the post-flame region, $\Delta\lambda_{opt}$ was selected for all temperature evaluations in this study, with wavelengths >700 nm having negligible impact on the residual in the post-flame region.

Strictly, this residual analysis does not uniquely prove wavelength-independent emissivity, since spectral emissivity variations may partly compensate changes in the fitted temperature. A sensitivity analysis with different low-order polynomial descriptions of emissivity [31] indicated that the resulting temperature ambiguity remains within the uncertainty range discussed below.

The temperature determination is subject to several sources of uncertainty. Temporal fluctuations in particle number density and slight motion of the reaction zone lead to variations in the measured spectra and thus in the inferred temperature. The reported temperature at each probing position corresponds to the mean of multiple spectra, while the standard deviation represents the statistical uncertainty, amounting to less than 5% near the reaction front and up to 10% in the post-flame region. The detected signal originates from a finite probe volume defined by the imaging optics and the pinhole aperture, which is small compared to the characteristic flame dimensions; projection effects are therefore expected to be minor. Due to the non-linear dependence of thermal radiation on temperature described by Planck's law, the detected emission is inherently biased toward the hottest particles within the probe volume. Including systematic uncertainties such as the determination of $C(\lambda)$, the cumulative uncertainty of the multispectral pyrometry for particle temperature quantification is estimated to be approx. 5% to 15%. This range also covers the temperature ambiguity associated with possible wavelength-dependent emissivity within the selected fitting interval. Despite this uncertainty and the inherent bias towards higher temperatures, the measurements reveal consistent trends with the applied flame boundary conditions, as discussed in the following sections.

2.3. Iron dust burner of Bunsen-type

In this study, the iron dust burner of Bunsen-type introduced by Fedoryk et al. [16] is employed, enabling the stabilization of self-sustained, laminar iron dust flames. A homogeneous, steady-state aerosol of micron-sized iron particles is generated using an air-knife seeder, adapted from Goroshin et al. [33]. The iron powder is pneumatically dispersed by accelerating the oxidizer gas through a narrow slit, while a piston continuously feeds the powder through a central tube, ensuring stable operation. A surrounding air coflow shields the flame. The mass flows of both the coflow and the oxidizer gas, *i.e.*, synthetic N_2/O_2 mixtures, are controlled by thermal mass flow controllers. Further details and a schematic of the iron dust burner are provided in Ref. [2].

The burner was mounted on a motorized three-axis traversing system, enabling precise 3D positioning of the probe volume for temperature measurements and LOS *in situ* XAS at different heights and radial locations. The flame was enclosed in a housing connected to the particle extraction system to minimize external disturbances. The housing featured X-ray access openings covered with 50 µm thick polyimide foil for XAS and a SiO_2 window positioned at 90° for multispectral pyrometry, see Fig. 2.

2.4. Investigated iron dust flames

Six laminar iron dust flames of Bunsen-type were investigated, as summarized in Table 1. All flames were operated with a mean outlet velocity of 40 cm s^{-1} and a constant coflow of air. Representative flame images are shown in Fig. 2; the investigated ROI is additionally indicated.

The spherical, dense iron particles, see Fig. 2, exhibited a median diameter of $D_{50} = 5.5$ µm, determined as described in Ref. [34]; the corresponding size distribution is given in Ref. [2].

3. Results & discussion

This section presents the results of spatially resolved iron (oxide) phase mapping and multispectral pyrometry, showing how the oxygen concentration in the oxidizer and the equivalence ratio influence particle temperature and phase evolution.

3.1. Influence of oxygen concentration in the oxidizer

The effect of oxygen concentration in the oxidizer on particle temperature and phase evolution was examined under stoichiometric conditions, see Table 1. Fig. 4 presents the reconstructed 2D temperature maps for flames #2 and #4 to #6, highlighting the systematic change in temperature distribution with increasing oxygen concentration in the oxidizer. The dashed black lines mark the flame front as determined from flame imaging, while white regions indicate areas where no

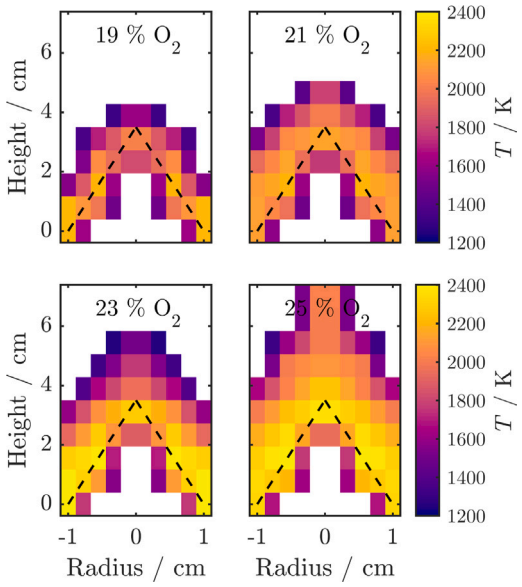

Fig. 4. 2D temperature maps reconstructed from multispectral pyrometry data using Planck's law fits for flames #2 and #4 to #6, illustrating the effect of increasing oxygen concentration in the oxidizer from 19 vol.% to 25 vol.% at $\Phi = 1.0$. White regions indicate areas where no temperature could be evaluated from the spectral data due to insufficient emission intensity. The dashed black lines mark the flame front derived from flame imaging data.

temperature could be evaluated due to insufficient spectral emission intensity I_λ.

Fig. 4 reveals that, for all oxygen concentrations, the highest temperatures are located in a narrow band around the reaction zone, *i.e.*, in the vicinity of the dashed black line. This observation is consistent with the initial oxidation step $Fe + 0.5\,O_2 \longrightarrow FeO$, and confirms that a major fraction of the total reaction enthalpy per iron atom is released during this first conversion. With increasing oxygen concentration in the oxidizer, the mean temperature in the reaction zone rises slightly from about 2140 K at 19 vol.% and 21 vol.% O_2 to about 2350 K at 23 vol.% and 25 vol.% O_2; these temperatures fall within the range reported in recent studies, *e.g.*, [35,36]. This trend is consistent with oxygen enrichment: a higher O_2 volume fraction reduces the inert gas dilution of the reacting mixture at fixed global equivalence ratio, *i.e.*, $\Phi = 1.0$, thereby increasing the local adiabatic flame temperature and enhancing the rate of the initial $Fe + 0.5\,O_2 \longrightarrow FeO$ conversion. In the post-flame region, a slower temperature decay is observed at higher oxygen concentrations, and the hot zone extends further downstream. This suggests that heat release continues beyond the temperature maximum, likely due to continued particle oxidation toward higher iron oxide phases. During this stage, however, the heat release is insufficient to balance heat losses to the surrounding gas and sustain high particle temperatures. As a result, the particle temperature decreases despite ongoing oxidation reactions, a regime commonly referred to as reactive cooling [37]. Additional cooling may arise from mixing with the surrounding coflow. The overall structure of the 2D temperature maps and the corresponding absolute particle temperatures agree well with the numerical results for flame #2, 21 vol.% O_2 and $\Phi = 1.0$, reported by Hazenberg et al. [29].

Consistent with the temperature fields, increasing the oxygen concentration in the oxidizer results in a systematic shift of the iron (oxide) phase maps. Fig. 5 presents the spatially resolved molar fractions of Fe, FeO, and Fe_3O_4, reconstructed from the *in situ* XAS data using LCA and inverse Abel transformation for flames #2 and #4 to #6, ordered from top to bottom with increasing O_2 concentration from 19 vol.% to 25 vol.%. Independent of the O_2 concentration, metallic Fe dominates

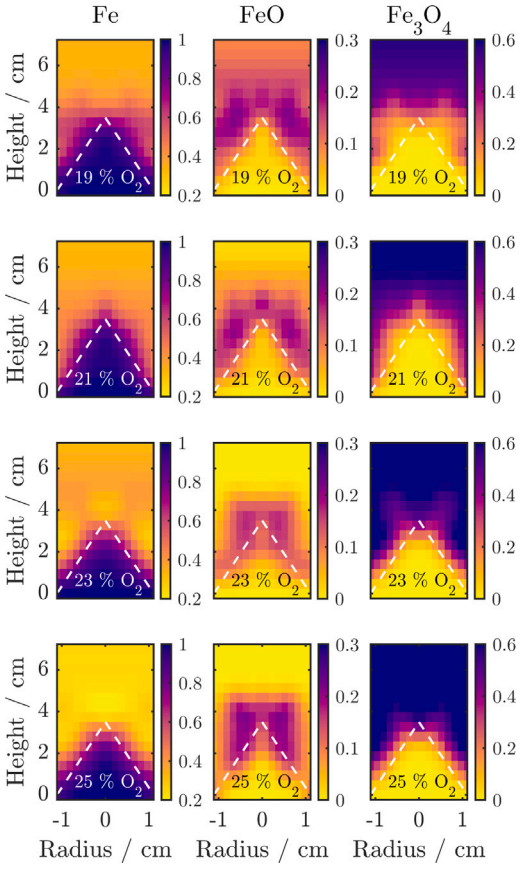

Fig. 5. 2D molar fraction maps of Fe, FeO, and Fe_3O_4, reconstructed from *in situ* XAS data using LCA and inverse Abel transformation, for flames #2 and #4 to #6, illustrating the effect of increasing oxygen concentration in the oxidizer from 19 vol.% to 25 vol.% at $\Phi = 1.0$. Note the different scaling of the colorbars. The dashed white lines indicate the flame front, derived from flame imaging data.

in the conical region upstream of the reaction front. The transition into the high-temperature region shown in Fig. 4 coincides with a decrease in the Fe fraction in all cases, as Fe particles traverse this zone and are progressively oxidized to FeO. This decline in the Fe fraction is most pronounced at higher oxygen concentrations, consistent with increased oxidation rates under elevated O_2 partial pressures and higher particle temperatures. The formation of FeO, the first oxide phase, coincides spatially with the region of maximum particle surface temperature, in agreement with Ref. [1]. In all flames, the FeO fraction peaks near the reaction front and decreases downstream as oxidation proceeds towards Fe_3O_4. Under these conditions, Fe_3O_4 forms in the post-flame region, where it is thermodynamically stable [1]. Its fraction increases with oxygen enrichment.

As evident from the 2D maps of iron (oxide) phases and temperature shown in Figs. 4 and 5, higher oxygen concentrations increase particle temperatures and extend the high-temperature region detectable by multispectral pyrometry downstream; corresponding centerline profiles are provided in the Supplementary Material. Under sub-air and air conditions, temperature evaluation was limited to 4 cm and 5 cm, respectively, due to insufficient spectral emission intensity further downstream. Consistent with the iron (oxide) phase maps, increasing O_2 concentration shifts the decrease in the Fe fraction toward lower flame heights, indicating faster conversion. However, given the constant mean outlet velocity and the increase in laminar burning velocity with oxygen enrichment [18,38], the resulting minor flame shortening may also contribute to this shift. Accordingly, the decrease

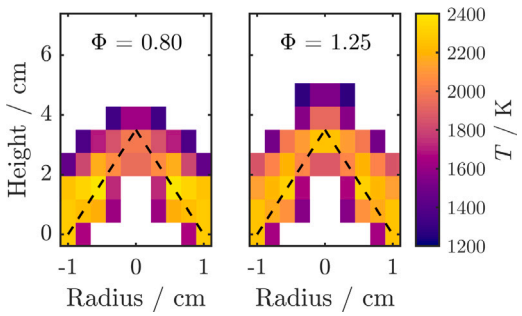

Fig. 6. 2D temperature maps reconstructed from multispectral pyrometry data using Planck's law fits for flames #1 and #3. Both flames were operated with air as oxidizer at $\Phi = 0.8$ and 1.25, respectively. The temperature field of the stoichiometric flame #2 is given in Fig. 4, including an explanation of white regions and dashed black lines.

in the Fe fraction and the upstream shift in the FeO peak position do not exclusively reflect accelerated oxidation kinetics. FeO forms slightly downstream of the reaction front, with its onset moving to lower flame heights as the oxygen concentration increases, while its peak fraction remains nearly unchanged. Further downstream, FeO is progressively converted to Fe_3O_4. At higher oxygen concentrations, this conversion is nearly complete within the ROI, whereas at 19 vol.% O_2 a residual FeO fraction of about 0.1 remains. Correspondingly, Fe_3O_4 appears at lower flame heights and reaches higher maximum fractions with increasing oxygen concentration. Overall, the iron (oxide) phase evolution follows the temperature field and its dependence on oxygen concentration.

Consistent with the temperature fields and phase evolution, increasing the oxygen concentration also increases nanoparticle formation. As shown in Ref. [2] for identical flames, higher O_2 concentrations lead to a marked increase in nanoparticle number concentration, while the shape of the size distribution remains largely unchanged. The elevated peak temperatures observed here likely promote iron vaporization in the reaction zone and thereby intensify the formation of gas-borne nanoparticles. Further downstream, the decrease in nanoparticles suspended in the gas phase is governed by hetero-coagulation with micron-sized particles.

3.2. Influence of equivalence ratio

In this section, the influence of equivalence ratio on particle temperature and phase evolution is discussed.

Fig. 6 shows the reconstructed temperature fields for the rich and lean flames, *i.e.*, $\Phi = 0.8$ and 1.25, while the stoichiometric reference case is given in Fig. 4. The flame front is indicated by dashed black lines. Overall, the temperature fields are very similar for all three conditions. Mean temperatures in the reaction zone agree within the experimental uncertainty of the multispectral pyrometry. Although the lean flame exhibits the highest peak temperature, consistent with previous studies [39,40], the differences relative to the stoichiometric and rich cases remain small and close to the measurement uncertainty, in agreement with Ref. [41]. Overall, no significant change in the spatial temperature distribution is observed when varying the equivalence ratio within the investigated range. The small differences may reflect compensating effects: richer mixtures contain more particles and may lead to greater heat release during oxidation but also exhibit stronger radiative losses, whereas lean conditions provide more oxidizer for faster particle oxidation but have a lower particle number concentration, *i.e.*, less fuel available for heat release.

In contrast to the temperature fields, the oxidation state of iron shows a noticeable dependence on the equivalence ratio. Fig. 7 shows spatially resolved molar fractions of Fe, FeO, and Fe_3O_4, reconstructed

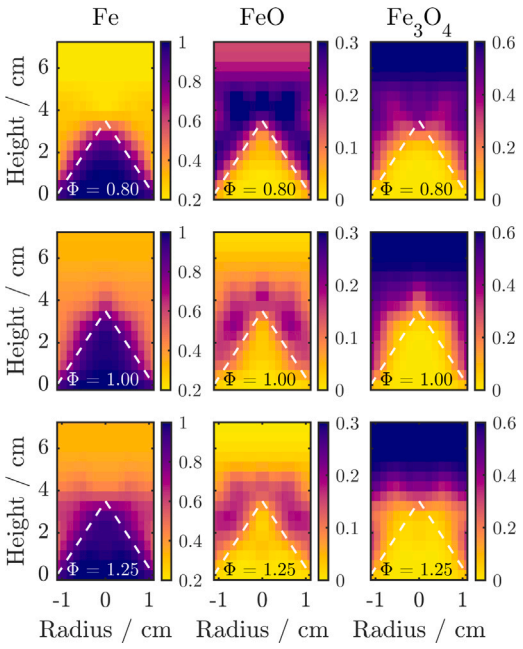

Fig. 7. 2D molar fraction maps of Fe, FeO, and Fe_3O_4, reconstructed from *in situ* XAS data using LCA and inverse Abel transformation, for flames #1 to #3. All flames were operated with air as oxidizer at $\Phi = 0.8$, 1.0, and 1.25, respectively. Note the different scaling of the colorbars. The dashed white lines indicate the flame front, derived from flame imaging data.

from the measurement points using LCA and inverse Abel transformation for the three flames with $\Phi = 0.8, 1.0$ and 1.25, ordered from top to bottom.

Independent of the equivalence ratio, metallic Fe dominates in the conical region before the micron-sized particles reach the reaction zone. As the particles travel through it, the Fe fraction decreases in all cases, with the strongest decline under lean conditions with $\Phi = 0.8$, consistent with higher oxidizer availability. As the equivalence ratio increases toward stoichiometric and rich conditions, more Fe remains, indicating a reduced overall oxidation degree. This trend agrees with the *ex situ* analysis of downstream-sampled particles reported in Ref. [20]. As discussed previously, FeO forms rapidly via the initial oxidation step $Fe + 0.5\,O_2 \longrightarrow FeO$ and is confined to the flame front. Regardless of the equivalence ratio, the FeO fraction peaks near this region and subsequently decreases due to further oxidation according to $3\,FeO + 0.5\,O_2 \longrightarrow Fe_3O_4$. Fe_3O_4, the thermodynamically most stable oxide under these conditions, *i.e.*, at a molar oxygen-to-iron ratio of less than about 1.35 depending on temperature [1], forms further downstream and is slightly more pronounced under lean conditions. Overall, the temperature field and spatial distribution of iron (oxide) phases appear to vary only slightly with equivalence ratio. The observed differences may mainly reflect changes in particle loading rather than in the underlying reaction sequence.

4. Concluding remarks

This study presents the coupled *in situ* quantification of spatially resolved iron (oxide) phase evolution and particle temperature in laminar iron dust flames using synchrotron XAS combined with multispectral pyrometry. The correlated thermal and chemical state information enables mechanistic interpretation of oxidation pathways under well-defined flame conditions. The study provides the following key findings:

i. The combined application of spatially resolved *in situ* XAS and multispectral pyrometry establishes a non-intrusive diagnostic framework enabling correlated quantification of iron (oxide) phase evolution and particle temperature.
ii. Oxidation proceeds in a two-step sequence, characterized by rapid conversion of Fe to FeO in the reaction front, followed by subsequent oxidation to Fe_3O_4 in the post-flame region.
iii. Higher oxygen concentrations increase particle temperatures and shift the oxide phase distribution toward Fe_3O_4, while the FeO peak fraction remains confined to the reaction front; variations in global stoichiometry, *i.e.*, equivalence ratio Φ, within the investigated range have only minor effects on the temperature field and phase distribution.
iv. The coupled temperature–phase measurements provide a benchmark data set for validating reaction mechanisms and multiphase combustion models and, together with the nanoparticle size distributions reported in Ref. [2], establish a consistent experimental framework linking particle temperature, phase composition, and nanoparticle formation.

CRediT authorship contribution statement

Fabian P. Hagen: Writing – original draft, Visualization, Software, Project administration, Investigation, Formal analysis, Conceptualization. **Lukas Braun:** Writing – review & editing, Investigation, Formal analysis, Conceptualization. **Dmitry E. Doronkin:** Writing – review & editing, Project administration, Investigation, Conceptualization. **Malte Seitz:** Writing – review & editing, Investigation. **Michal Fedoryk:** Writing – review & editing, Investigation. **Björn Stelzner:** Writing – review & editing, Project administration. **Jan-Dierk Grunwaldt:** Writing – review & editing, Supervision, Funding acquisition. **Dimosthenis Trimis:** Writing – review & editing, Supervision, Funding acquisition.

Declaration of competing interest

The authors declare that they have no known competing financial interests or personal relationships that could have appeared to influence the work reported in this paper.

Acknowledgments

This work was conducted within the Clean Circles cluster project, supported by the Strategy Fund of the KIT Presidium. The research also contributes to the Helmholtz Association's MTET program Resource and Energy Efficiency, Anthropogenic Carbon Cycle (38.05.01). We acknowledge DESY (Hamburg, Germany), a member of the Helmholtz Association HGF, for the provision of experimental facilities. Parts of this research were carried out at PETRA III. Data was collected using P64 beamline operated by DESY Photon Science. We would like to thank Dr. Aleksandr Kalinko (DESY), Dr. Wolfgang Caliebe (DESY), Marc Viehweger (DESY) and Jonas H. Müller (KIT) for assistance during the experiments. Beamtime was allocated for proposals I-20230884 and I-20250369.

Appendix A. Supplementary data

Supplementary material related to this article can be found online at https://doi.org/10.1016/j.proci.2026.106244.

References

[1] A. Sperling, M.P. Deutschmann, D. Ning, J. Spielmann, T. Li, U.I. Kramm, H. Nirschl, B. Böhm, A. Dreizler, Oxidation progress and inner structure during single micron-sized iron particles combustion in a hot oxidizing atmosphere, Fuel 381 (2025) 133147.
[2] F.P. Hagen, J.H. Müller, H. Störmer, B. Stelzner, Y.M. Eggeler, D. Trimis, On nanoparticles in iron dust flames of Bunsen-type: Evolution of size distribution and hetero-coagulation with micron-sized particles, Fuel 398 (2025) 135598.
[3] J. Bergthorson, S. Goroshin, M. Soo, P. Julien, J. Palecka, D. Frost, D. Jarvis, Direct combustion of recyclable metal fuels for zero-carbon heat and power, Appl. Energy 160 (2015) 368–382.
[4] J.M. Bergthorson, Recyclable metal fuels for clean and compact zero-carbon power, Prog. Energy Combust. Sci. 68 (2018) 169–196.
[5] P. Debiagi, R. Rocha, A. Scholtissek, J. Janicka, C. Hasse, Iron as a sustainable chemical carrier of renewable energy: Analysis of opportunities and challenges for retrofitting coal-fired power plants, Renew. Sustain. Energy Rev. 165 (2022) 112579.
[6] D. Ning, Y. Li, T. Li, B. Böhm, A. Dreizler, Size-resolved ignition temperatures of isolated iron microparticles, Combust. Flame 270 (2024) 113779.
[7] D. Ning, Y. Shoshin, J. van Oijen, G. Finotello, L. de Goey, Burn time and combustion regime of laser-ignited single iron particle, Combust. Flame 230 (2021) 111424.
[8] D. Ning, T. Li, J. Mich, A. Scholtissek, B. Böhm, A. Dreizler, Multi-stage oxidation of iron particles in a flame-generated hot laminar flow, Combust. Flame 256 (2023) 112950.
[9] S. Li, J. Huang, W. Weng, Y. Qian, X. Lu, M. Aldén, Z. Li, Ignition and combustion behavior of single micron-sized iron particle in hot gas flow, Combust. Flame 241 (2022) 112099.
[10] D. Ning, Y. Shoshin, M. van Stiphout, J. van Oijen, G. Finotello, P. de Goey, Temperature and phase transitions of laser-ignited single iron particle, Combust. Flame 236 (2022) 111801.
[11] T. Li, F. Heck, F. Reinauer, B. Böhm, A. Dreizler, Visualizing particle melting and nanoparticle formation during single iron particle oxidation with multi-parameter optical diagnostics, Combust. Flame 245 (2022) 112357.
[12] J. Hameete, M. Abdallah, L. Thijs, T. Homan, X. Mi, N. Dam, L. de Goey, Particle-resolved hyperspectral pyrometry of metal particles, Combust. Flame 264 (2024) 113435.
[13] D. Ning, Y. Shoshin, J. van Oijen, G. Finotello, P. de Goey, Size evolution during laser-ignited single iron particle combustion, Proc. Combust. Inst. 39 (2023) 3561–3571.
[14] T. Li, B.-D. Nguyen, Y. Gao, L. Elsässer, D. Ning, A. Scholtissek, A.C. van Duin, C. Hasse, B. Böhm, Critical nanoparticle formation in iron combustion: single particle experiments with in-situ multi-parameter diagnostics aided by multi-scale simulations, Fuel 404 (2026) 136303.
[15] D. Chang, L.C. Thijs, A. Panahi, X. Mi, J.M. Bergthorson, Y.A. Levendis, Effects of oxygen concentration on nanoparticle formation during combustion of iron powders, Fuel 397 (2025) 135366.
[16] M. Fedoryk, B. Stelzner, S. Harth, D. Trimis, Experimental investigation of the laminar burning velocity of iron-air flames in a tube burner, Appl. Energy Combust. Sci. 13 (2023) 100111.
[17] M. McRae, P. Julien, S. Salvo, S. Goroshin, D.L. Frost, J.M. Bergthorson, Stabilized, flat iron flames on a hot counterflow burner, Proc. Combust. Inst. 37 (2019) 3185–3191.
[18] T. Krenn, T. Li, J. Hebel, B. Böhm, A. Dreizler, Evaluation of a novel measurement method for the laminar burning speed in laminar lifted iron dust flames, Fuel 366 (2024) 131266.
[19] M. Hulsbos, R. Hermanns, R. Bastiaans, L. de Goey, The laminar burning velocity of hybrid iron-methane-air flames, Combust. Flame 279 (2025) 114274.
[20] S. Buchheiser, M.P. Deutschmann, F. Rhein, A. Allmang, M. Fedoryk, B. Stelzner, S. Harth, D. Trimis, H. Nirschl, Particle and phase analysis of combusted iron particles for energy storage and release, Materials 16 (2023).
[21] L. Choisez, N.E. van Rooij, C.J. Hessels, A.K. da Silva, I.R.S. Filho, Y. Ma, P. de Goey, H. Springer, D. Raabe, Phase transformations and microstructure evolution during combustion of iron powder, Acta Mater. 239 (2022) 118261.
[22] A. Boubnov, H. Lichtenberg, S. Mangold, J.-D. Grunwaldt, Identification of the iron oxidation state and coordination geometry in iron oxide- and zeolite-based catalysts using pre-edge XAS analysis, J. Synchrotron Radiat. 22 (2015) 410–426.
[23] B.B. Sarma, J.-D. Grunwaldt, Operando spectroscopy to understand dynamic structural changes of solid catalysts, Chimia 78 (2024) 288–296.
[24] W.A. Caliebe, V. Murzin, A. Kalinko, M. Görlitz, High-flux XAFS-beamline P64 at PETRA III, AIP Conf. Proc. 2054 (2019) 060031.
[25] B. Bornmann, J. Kläs, O. Müller, D. Lützenkirchen-Hecht, R. Frahm, The quick EXAFS setup at beamline P64 at PETRA III for up to 200 spectra per second, AIP Conf. Proc. 2054 (2019) 040008.
[26] H. Franz, O. Leupold, R. Röhlsberger, S. Roth, O. Seeck, J. Spengler, J. Strempfer, M. Tischer, J. Viefhaus, E. Weckert, T. Wroblewski, Technical report: PETRA III: DESY's new high brilliance third generation synchrotron radiation source, Synchrotron Radiat. News 19 (2006) 25–29.

[27] X. Wen, A. Scholtissek, J. van Oijen, J. Bergthorson, C. Hasse, Numerical modeling of pulverized iron flames in a multidimensional hot counterflow burner, Combust. Flame 248 (2023) 112572.
[28] W.S. Ramaekers, T. Hazenberg, L. Thijs, D. Roekaerts, J. van Oijen, L. de Goey, The influence of radiative heat transfer on flame propagation in dense iron-air aerosols, Combust. Flame 272 (2025) 113848.
[29] T. Hazenberg, D. Braig, M. Fedoryk, J. Mich, F. Hagen, S. Harth, B. Stelzner, A. Scholtissek, D. Trimis, C. Hasse, Analyzing iron dust Bunsen flames using numerical simulations, Fuel 403 (2026) 136094.
[30] T. Hazenberg, D. Braig, J. Mich, A. Scholtissek, C. Hasse, Numerical analysis of the stability of iron dust Bunsen flames, Proc. Combust. Inst. 41 (2025) 105861.
[31] A. Araújo, Multi-spectral pyrometry – a review, Meas. Sci. Technol. 28 (2017) 082002.
[32] D.-X. Qu, J. Berry, N.P. Calta, M.F. Crumb, G. Guss, M.J. Matthews, Temperature measurement of laser-irradiated metals using hyperspectral imaging, Phys. Rev. Appl. 14 (2020) 014031.
[33] S. Goroshin, M. Bidabadi, J. Lee, Quenching distance of laminar flame in aluminum dust clouds, Combust. Flame 105 (1996) 147–160.
[34] M.P. Deutschmann, A. Sperling, E. Covini, B. Böhm, A. Dreizler, H. Nirschl, Single iron particle combustion - A morphology study of partially oxidized iron particles, Powder Technol. 445 (2024) 120102.
[35] P. Tóth, Y. Ögren, A. Sepman, P. Gren, H. Wiinikka, Combustion behavior of pulverized sponge iron as a recyclable electrofuel, Powder Technol. 373 (2020) 210–219.
[36] S. Jiménez, M. Mayoral, L. Romeo, Detailed physicochemical evolution of iron particles burnt under controlled, realistic conditions, Fuel 391 (2025) 134668.
[37] J. Mich, A.K. da Silva, D. Ning, T. Li, D. Raabe, B. Böhm, A. Dreizler, C. Hasse, A. Scholtissek, Modeling the oxidation of iron microparticles during the reactive cooling phase, Proc. Combust. Inst. 40 (2024) 105538.
[38] X. Liu, N. Hashimoto, Y. Xia, Q. Wang, Y. Konno, O. Fujita, Experimental investigation of oxygen concentration effects on spherical laminar flame propagation of micron-sized iron particle clouds, Combust. Flame 277 (2025) 114234.
[39] W. Prasidha, M. Baigmohammadi, Y. Shoshin, P. de Goey, Towards an efficient metal energy carrier for zero–emission heating and power: Iron powder combustion, Combust. Flame 268 (2024) 113655.
[40] W. Prasidha, M. Baigmohammadi, Y. Shoshin, P. de Goey, Optimizing iron powder combustion: Influence of particle size on flame stability, nanoparticle formation, and nitric oxide emission, Combust. Flame 275 (2025) 114068.
[41] M. Baigmohammadi, W. Prasidha, N.C. Stevens, Y.L. Shoshyn, T. Spee, P. de Goey, Towards utilization of iron powders for heating and power, Appl. Energy Combust. Sci. 13 (2023) 100116.